

Provided for non-commercial research and education use.  
Not for reproduction, distribution or commercial use.



(This is a sample cover image for this issue. The actual cover is not yet available at this time.)

**This article appeared in a journal published by Elsevier. The attached copy is furnished to the author for internal non-commercial research and education use, including for instruction at the authors institution and sharing with colleagues.**

**Other uses, including reproduction and distribution, or selling or licensing copies, or posting to personal, institutional or third party websites are prohibited.**

**In most cases authors are permitted to post their version of the article (e.g. in Word or Tex form) to their personal website or institutional repository. Authors requiring further information regarding Elsevier's archiving and manuscript policies are encouraged to visit:**

**<http://www.elsevier.com/copyright>**

Contents lists available at [SciVerse ScienceDirect](http://www.sciencedirect.com)

# Earth and Planetary Science Letters

journal homepage: [www.elsevier.com/locate/epsl](http://www.elsevier.com/locate/epsl)

## Remelting in caldera and rift environments and the genesis of hot, “recycled” rhyolites

A.G. Simakin <sup>a,\*</sup>, I.N. Bindeman <sup>b</sup><sup>a</sup> Institute of Physics of the Earth, Russian Academy of Sciences, Moscow, Russia<sup>b</sup> Department of Geological Sciences, 1272 University of Oregon, Eugene, OR 97403, USA

### ARTICLE INFO

#### Article history:

Received 21 July 2011

Received in revised form

5 April 2012

Accepted 7 April 2012

Editor: T.M. Harrison

#### Keywords:

convection

melting

high silica rhyolites

numerical modeling

magma rheology

### ABSTRACT

Large and small volume rhyolites are generated in calderas and rift zones, inheriting older and isotopically diverse crystal populations from their volcanic predecessors. Low- $\delta^{18}\text{O}$  values in many of these rhyolites suggest that they were derived from the remelting of solid, hydrothermally altered by meteoric water protoliths that were once close to the surface, but become buried by caldera collapse or rifting. These rhyolites persist for millions of years in these environments with little evidence of coeval basalts. We present a series of numerical experiments on convective melting of roof-rocks by the underplated by near liquidus to superheated silicic melts, generated at the base of the chamber by basaltic intrusions in shallow crustal conditions. We used a range of temperatures and compositions, an appropriate phase diagram with a defined extended eutectic zone appropriate for these environments, varied sill thickness, viscosity of the boundary layer, and considered hydrothermal and lower boundary heat losses. The goal was to estimate melting rates and mechanisms, define conditions that are required for efficient and rapid remelting in the upper crust, quantitatively describe novel details of the dynamics of convecting melting, and compare it to the earlier parametric and numerical treatments of roof melting by underplating. Resolution of numerical experiments allowed us to track mixed thermal and two-phase plume-like convection in silicic magma with a bulk viscosity of  $10^{4.5}$ – $10^{5.5}$  Pa s. The following results were obtained: (1) remarkably fast melting/magma generation rates of many meters per year, (2) intrinsic inhomogeneities in the roof accelerates convection and melting rates via rapid gravitational settling of refractory blocks and exposing detachment scars to the melting front, (3) due to rapid melting, hydrothermal heat loss through the roof, and conductive heat dissipation through the bottom are less important on melting timescales. (4) Convective melting is capable of digesting cold roof-rocks, with high assimilation degrees, which are primarily controlled by sill thickness and roof-rock temperature: thin 10 m sills are able to digest 40% of the initially hot roof-rock  $T=650$  °C roof-rock, but > 100 m sills achieve the same level of bulk digestion with  $T=400$  °C roof-rocks. The proposed model can explain the origin of hot (above 800–850 °C), crystal-poor, “recycled” rhyolites in calderas and rift zones. It can also explain the generation of large, supervolcanic rhyolite volumes through remelting of their erupted and subvolcanic predecessors on rapid timescales, dictated by their zoned and disequilibrium crystalline cargo.

© 2012 Elsevier B.V. All rights reserved.

## 1. Introduction

### 1.1. Large-volume silicic magma genesis

Understanding the origin of large-volume rhyolites, and especially high-silica rhyolites (HSR), is important for several reasons. First, huge volume silica rhyolites are the most evolved and multiply saturated silicate melts on Earth. They lie close to the eutectic on classic granite melting diagrams, and demonstrate

\* Corresponding author.

E-mail addresses: [simakin@ifz.ru](mailto:simakin@ifz.ru) (A.G. Simakin), [bindeman@uoregon.edu](mailto:bindeman@uoregon.edu) (I.N. Bindeman).

significant changes in melt fraction with small increases in temperature (Bowen, 1928; Tuttle and Bowen, 1958; Brugger et al., 2003). Second, these are the highest viscosity silicate liquids, yet they erupt in large volumes and form calderas (Lipman, 1984; Anderson et al., 2000; Wark et al., 2007). Third, phase equilibria, melt inclusion studies, their crystal-poor (0–25%) character, and association with calderas all suggest that they are stored as hot, near liquidus liquids at relatively shallow depths of a few kilometers (Wallace et al., 1999; Hildreth and Wilson, 2007; Vazquez et al., 2009; Girard and Stix, 2010). Fourth, rapid formation and eruption of such large ‘supervolcanic’ volumes of rhyolite presents one of the most extreme geologic hazards to society.

Recent work at Yellowstone, the Snake River Plain and elsewhere demonstrates that many individual rhyolitic units with volumes ranging from a few km<sup>3</sup> to ~2000 km<sup>3</sup> represent low- $\delta^{18}\text{O}$  magmas (Bindeman et al., 2001, 2006, 2008; Borroughs et al., 2005; Ellis et al., 2010; Watts et al., 2010, 2011). This suggests that this precursor rocks have been cooled below the rhyolitic solidus to develop open cracks for meteoric water percolation and massive  $\delta^{18}\text{O}$  exchange (Fig. 1) in shallow, water-dominated environments before being remelted. Based on simple mass balance of the major element oxygen, the genesis of these rhyolites requires tens of percent assimilation of (or derivation from) hydrothermally altered precursor rhyolites. Upon remelting, the final (and hot) low- $\delta^{18}\text{O}$  rhyolites inherit crystals from assimilated rocks of variable  $\delta^{18}\text{O}$  compositions. The “shallow” low- $\delta^{18}\text{O}$  value serves to fingerprint subaerial meteoric waters. If altering waters were higher in  $\delta^{18}\text{O}$  (e.g., seawater), high- $\delta^{18}\text{O}$  magmas would be predicted to arise because the inferred process of remelting remains the same, implying that the advocated genesis mechanism is not specific for low- $\delta^{18}\text{O}$  rhyolites alone, but applies to all silicic magma petrogenesis in caldera and rift environments. Caldera collapse events are the most efficient geologic mean to bring these hydrothermally altered rhyolites deeper near the source of heat of the magma chambers (Fig. 1).

The best petrogenetic line of evidence from these ‘recycled’ rhyolites, which range in size from few to > 2000 km<sup>3</sup> of cubic kilometers, comes from isotopically zoned xenocrysts of quartz and zircon. Examples include small volume (> 40 km<sup>3</sup>) rhyolites of Yellowstone and Iceland (Bindeman et al., 2008, 2012; Carley et al., 2011), many voluminous rhyolites of SRP including the 1800 km<sup>3</sup> Kilgore Tuff of the Heise volcanic field (Watts et al., 2011), and the

900 km<sup>3</sup> Ammonia Tanks Tuff from the Timber Mt caldera (Bindeman et al., 2006). Zircons in these rhyolites survived hydrothermal alteration were buried with their country rocks, and got surrounded by low  $\delta^{18}\text{O}$  melt after caldera collapse (Fig. 1). Time estimates based on their U–Pb, U–Th–Pb vs Ar–Ar ages, rates of diffusion and solution–reprecipitation (Bindeman et al., 2008, 2012), and crystal size distributions (Simakin and Bindeman, 2008) are on the order of 10<sup>2</sup>–10<sup>4</sup> yr. Given this maximum time estimate and the eruptive volume of the units, magma generation rates range from 0.04 km<sup>3</sup>/yr (e.g., Yellowstone’s Upper Basin Member lavas) to 0.1 km<sup>3</sup>/yr (e.g., Heise’s Kilgore Tuff and Timber Mt.’s Ammonia Tanks Tuff). It is remarkable that these “recycled” rhyolites maintain high temperatures of > 800 °C, and in some cases, drier and more primitive low silica, low  $\delta^{18}\text{O}$  rhyolites and dacites have temperatures up to ~1000 °C (Nash et al., 2006).

### 1.2. Current theoretical models on the depths and mechanisms of silicic magma generation by injection and underplating

A seminal paper by Huppert and Sparks (1988) presented a parametric study of granite generation by crustal melting following contact with underlying basaltic magma. These authors demonstrated theoretically and confirmed in experiments the importance of heat flux vs temperature contrasts for Newtonian liquid in a simulation of melting processes. They showed that there is a large potential for basalts to generate rhyolitic magmas in the upper silicic crust. A similar parametric model was recently used by Huber et al. (2010) to estimate efficiency of the mobilization of partial melts by underplating. Recent papers by Petford and Gallagher (2001), Annen and Sparks (2002), and Annen et al. (2006) with a 1D model, and Dufek and Bergantz (2005) with a 2D model, consider essential thermophysics of the crustal melting. In these studies, heat transfer equations are solved taking into account the details of heat of fusion, but without consideration of the complicated details of convective granitic melt segregation and vertical transport. These and other authors prefer melting to take place in the deep crust where ambient temperatures are close to the solidus, geothermal gradients are high, and favor slow, incremental batholithic magma assembly spanning millions of years, consistent with geochronological and geological data on batholith segregation timescales (Coleman et al., 2004; Glazner et al., 2004).

However, isotopic evidence presented above strongly suggests that small and large volumes of hot rhyolitic magmas can also be generated rapidly in the shallow crust (Fig. 1), which seemingly contrast deep, slow generation, or long mush extraction timescales. There is no heat limitation either: at realistic basaltic magma intrusion rates of 0.001–0.1 km<sup>3</sup>/yr (Zellmer et al., 2005) similar amounts of silicic magma can be generated (and may erupt in similar volumes) in the middle-upper crust over < 10<sup>5</sup> yr.

Evaluation of the efficiency of silicic magma generation in the upper crust is hindered by the complexity of convective heat transfer. Convective cooling and crystallization has been the subject of numerous theoretical and experimental publications (Davaille and Jaupart, 1993; Brandeis and Marsh, 1990; Lenardic and Moresi, 2003; Carrigan, 1988). However, numerical convective melting is studied less comprehensively. Only in numerical modeling, can one properly account for phase diagrams, temperature and crystal content dependence of melt viscosities, and details of heat transfer and melting.

### 1.3. Formulation of tasks for this work

In this paper we attempted to numerically model rhyolite genesis by remelting after caldera collapse, in which remelting of previously erupted and buried rhyolites is caused by the heat of hotter rhyolites coming from greater depths, possibly after being generated by basalt

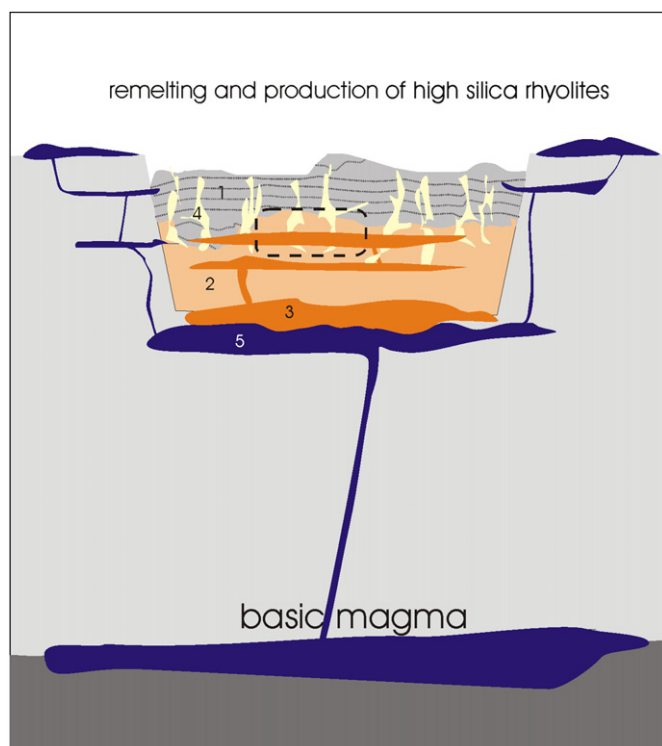


**Fig. 1.** Schematic view of the shallow remelting in the caldera settings. Basic magma (5) from the mantle causes formation of hot low-silica rhyolites and dacites, (3) at the base of caldera block. These hot often superheated silicic magmas ascend, spread laterally, and melt buried pyroclastic (1) and subvolcanic (2), hydrothermally altered rocks (4) formed in the previous eruptions, which may contain significant proportion of volcanic glass. Low density caldera rocks serve as density filter, which prevents basalt from eruption within caldera, but causes it to accumulate and release heat under caldera. Dashed rectangle outlines the domain used in numerical simulations of this paper.

(Fig. 1) We consider superheated rhyolite (rather than dense basalt) as the melt that delivers heat and causes roof-rock melting, because of the geochemical evidence from silicic caldera complexes, which demonstrate the eruption of high-silica rhyolitic compositions throughout the pre-caldera, caldera and post-caldera eruptive sequences. These rocks often preserve “delicately” high Rb/Sr and other ratios (e.g., Vazquez and Reid, 2002) that would have been severely modified by mixing with basalt. Only the deepest eruptive draw-downs during caldera-formation tap low-silica-rhyolitic, dacitic and sometimes more mafic, crystal rich magma, presumably located near the bottom of the silicic magma reservoirs, as is evidenced by many zoned ignimbrite eruptions (Lipman, 1984). The simulations involve a realistic phase diagram with variable compositions (quartz undersaturated vs quartz oversaturated), roof-rock, and underlying magma temperatures. The simulations are used to estimate the conditions of melting, calculate magma production and convective heat transfer rates, describe melting dynamics through time and the evolution of temperature gradients and melting, and make estimates of the efficiency of the melting and assimilation processes.

## 2. Setting up the numerical model of melting by underplating

### 2.1. Conservation equations

The numerical model includes solving two constitutive parts of the Navier–Stokes equation reduced for low  $Re$  flows (creep flow approximation), conservation of the energy equation, accounting for crystallization in the volume, and the incompressibility conditions. An effective viscosity as a function of temperature and strain rate at a crystal content above the lock threshold ( $\varepsilon > 0.55$ ) was used.

$$\begin{aligned} -\frac{\partial p}{\partial x} + 2\frac{\partial}{\partial x}(\eta(T)\frac{\partial u_x}{\partial x}) + \frac{\partial}{\partial y}(\eta(T)(\frac{\partial u_x}{\partial y} + \frac{\partial u_y}{\partial x})) &= 0 \\ \rho g - \frac{\partial p}{\partial y} + 2\frac{\partial}{\partial y}(\eta(T)\frac{\partial u_y}{\partial y}) + \frac{\partial}{\partial x}(\eta(T)(\frac{\partial u_y}{\partial x} + \frac{\partial u_x}{\partial y})) &= 0 \\ \nabla u = \frac{\partial u_i}{\partial x_i} &= 0 \end{aligned} \quad (1)$$

Conservation of the energy equation is formulated in enthalpy form to account for volume phase transitions without relative phase motion. For simplicity we also neglect the heat capacity difference between melt and solids (effective heat capacity approximation) that yields:

$$\begin{aligned} \partial H / \partial t &= \lambda \Delta T - c_p \rho u_i \nabla T \\ H &\approx \rho \varepsilon_l(T) \Delta H_m + c_p \rho T \end{aligned} \quad (2)$$

where  $\lambda$  is the heat transfer coefficient ( $\lambda = c_p \rho k_T$ ), and  $\varepsilon_l(T)$  is the volume fraction of the melt. Advective material transfer is described in Lagrangian coordinates moving with magma particles

$$\frac{DC}{Dt} = 0 \quad (3)$$

where  $C$  is weight fraction of quartz in rhyolitic melt (see Section 2.3.1 below). The Navier–Stokes equation was nondimensionalized with a linear scale equal to size of the element  $l_o$ , time  $l_o^2/k_T$ , and velocity  $k_T/l_o$ . Viscosity varies considerably, and therefore a reference viscosity  $\eta_o$  is used. Pressure is scaled on the  $\eta_o k_T/l_o^2$

$$-\frac{\partial p}{\partial x} + 2\frac{\partial}{\partial x}\left(\frac{\eta(T)}{\eta_o}\frac{\partial u_x}{\partial x}\right) + \frac{\partial}{\partial y}\left(\frac{\eta(T)}{\eta_o}\left(\frac{\partial u_x}{\partial y} + \frac{\partial u_y}{\partial x}\right)\right) = 0 \quad (4a)$$

$$\frac{\Delta \rho(T)}{\Delta \rho_o} Ra - \frac{\partial p}{\partial y} + 2\frac{\partial}{\partial y}\left(\frac{\eta(T)}{\eta_o}\frac{\partial u_y}{\partial y}\right) + \frac{\partial}{\partial x}\left(\frac{\eta(T)}{\eta_o}\left(\frac{\partial u_y}{\partial x} + \frac{\partial u_x}{\partial y}\right)\right) = 0 \quad (4b)$$

The local Rayleigh number  $Ra = \Delta \rho_o g l_o^3 / k_T \eta_o$  is used instead of global one (at linear scale equals the thickness of the liquid layer), and this approach is preferred since the thickness of the convective

layer is not well-defined due to viscosity increases at the upper thermal boundary layer, and expansion due to melting of the roof.

The heat balance equation is reformulated as

$$\partial T / \partial t \left(1 + \frac{d\varepsilon}{dT} \Delta T_c Ste\right) = \Delta T - u_i \nabla T \quad (5)$$

where Stefan number  $Ste = \Delta H_m / \Delta T_c \rho c_p$ , so that the multiplier at time derivative of the temperature can be interpreted as effective heat capacity  $c_{p,eff} = 1 + \varepsilon'_T \Delta T_c Ste$ .

This system of Eqs. (3)–(5) is solved with a finite element method (FEM) code written for this work. Bilinear elements are used to approximate the velocity field ( $u_x, u_y$ ) and temperature. A penalty method was applied to provide fluid incompressibility conditions, and advective material transfer was described with a marker technique (see, e.g., in Gerya, 2009). The viscous and gravity terms have been integrated numerically on the element subgrid ( $2 \times 2$ ). At the element size  $0.25 \times 0.25$  m this integration implies averaging of the magma properties in the domain of the size  $12.5 \times 12.5$  cm. Validation of the FEM code to evaluate flow velocities at a strong viscosities contrast was proved using an analytical solution (see Appendix A).

### 2.2. Initial and boundary conditions

The upper boundary of the solid rock layer is insulated, since it is far away from the melting and heating front on timescales of our experiments. Vertical boundaries are treated as symmetrical with respect to temperature  $\partial T / \partial x = 0$  and velocity  $\partial u_y / \partial x = 0$  ( $u_y = 0$ , in some experiments).

As we model melting of the silicic volcanic roof-rocks by underplating magmas in a simplified two-layer system (Fig. 1), we first consider heat transfer, convection, and melting processes occurring at the lower and upper boundaries of intruded melt, and discuss the relative importance of the bottom heat loss and hydrothermal cooling in the overall heat balance (e.g., Carrigan, 1988). A series of simulations involving convective magma sill in the thick framework of country rock result in formation of a stagnant cooled magma layer near the bottom of the sill (see movie in Suppl. material). Interestingly, similar stagnant bottom layer was observed in tank experiments of Jaupart and Brandeis (1986). Like in our numerical observations, these authors observed that this stagnant layer undergoes slow conductive crystallization from below and, that its upper boundary is partially penetrated by convective plumes from above (see movie in Suppl. material). We thus neglect slow heat loss through this stagnant bottom layer and set up a lower boundary that is thermally insulated and stress-free (see also Snyder, 2000 for similar approximation). Our comparison of the melting rates during the initial stage with an insulating bottom model and a model which does not have this constraint showed a difference of 1–3%. The estimated heat loss by hydrothermal circulation is also very small ( $< 3\%$ ) on the fast timescales involved compared to the energies of melting and crystallization processes in our models.<sup>1</sup>

Supplementary material related to this article can be found online at <http://dx.doi.org/10.1016/j.epsl.2012.04.011>.

<sup>1</sup> Hydrothermal contribution is important for slow convection and slowly cooling and crystallizing magma (Carrigan, 1988). It follows from the much larger magma convective heat fluxes associated with melting with rates of 10 m/yr (300–400 W/m<sup>2</sup>) as compared with average hydrothermal fluxes of 2 W/m<sup>2</sup> for Yellowstone (value from Carrigan, 1988). To test this we make several experiments with imposed heat flux condition (2 W/m<sup>2</sup>) on the outer horizontal boundary of computation domain and initial temperature gradient of 1°/m in the roof corresponding to this flux (at  $\lambda = 2$  W/m/o). Comparison with insulating upper boundary ( $T_o = 650$  °C,  $T_m = 940$  °C) gets decreasing of the initial melting rate on 2.5% due to hydrothermal cooling. In the further work we neglect this effect and use insulating upper boundary.

The size of the computational domain was varied to choose the appropriate resolution to model convection. Most calculations were done on the equispaced rectangular FEM grid with dimensions from  $61 \times 71$  to  $80 \times 80$  that proved to be adequate, and selected control runs were done on the bigger  $120 \times 180$  grid. Physical grid length varies from 25 to 15 cm with respective gravity and viscosity integration domains in the range of 12.5–7.5 cm. Therefore the total physical dimensions of the simulated systems varied from  $45 \times 30$  m to  $20 \times 20$  m, and this size is sufficient to capture all necessary physical constrains and physical processes.

First, at given magma layer dimensions, global Rayleigh number at the temperature difference  $\Delta T = T_s - T_m$  is sufficiently high  $Ra_s = 1 - 3 \times 10^7$  so that the convective heat flux does not depend on the layer thickness, but only on magma properties and  $\Delta T$ . This is a result which is well established theoretically, checked experimentally, and found to be widely used in practice (e.g., Turcotte and Schubert, 2002; Huppert and Sparks, 1988). Therefore further increase of the magma layer thickness will not affect instant melting rates at the given  $T_m$ , and doubling of the layer thickness in control runs had no effect on the melting rate. Resolution of the velocity field appears to be adequate to catch small, initially two-phase thermals developing on the melting front (see movie in Suppl. material).

Secondly, the computation domain size is sufficient to use a far field thermal boundary condition. As shown in Huppert and Sparks (1988) a steep exponential temperature gradient on the melting front has a length scale  $L = k_T / u_m \approx 6$  m (at  $k_T = 10^{-6} \text{ m}^2/\text{s}$  and  $u_m = 5 \text{ m/yr}$ ). Finally, we extend our results obtained in a small system for larger sills with simple heat balance estimates.

Initial temperature of the upper layer (roof-rock) ranged from 200 to 720 °C, while the underplating magma temperatures ranged from 800 to 940 °C. The upper limit of temperature is imposed by the requirements of the moderate viscosity to stay in petrologically reasonable  $\sim 10$  cm spatial resolution for convective plumes. To start the convection, low amplitude (about 1 °C) double periodic initial temperature distribution was imposed in the magma.

### 2.3. Material parameters

#### 2.3.1. Phase diagram approximation

Our melting phase diagram (Fig. 2) represents a linear approximation of the binary section in the Ab–Or–Qz system at  $P_{\text{H}_2\text{O}} = 1$  kbar (Tuttle and Bowen, 1958) through the cotectic minimum to the Qz apex. The composition is expressed via weight fraction of quartz in the Fsp–Qz binary, corresponding to variation of  $\text{SiO}_2$  contents in the range of 70–82 wt%, which encompasses a range from low- to high-silica rhyolites, to Qz-oversaturated compositions. For simplicity, feldspar is taken as  $\text{Ab}_{50}\text{Or}_{50}$ . The solid fraction (of Qz, Fsp or both at  $T < T_e$ ) is a nonlinear function of temperature at fixed bulk composition (Fig. 2), as melting involves the eutectic. In order to describe the eutectic region and avoid discontinuity where melt fraction drops to zero at specified constant temperature, we smoothed this transition in the finite temperature interval from  $T_e = 744$  to  $T_s = 715$  °C with the melt fraction following a linear dependence.

The melting diagram in Fig. 2 is displayed as a set of curves  $T_m(\epsilon_s)$  in the Quartz and Feldspar fields; bulk composition is a constant on each curve ( $X_{\text{Qz}} = 0.31; 0.26; 0.21; 0.16$  and  $X_{\text{Qz}} = 0.41; 0.46; 0.51; 0.56$  in the Fsp and Qz fields, respectively). The composition of the underplating magma was always  $X_{\text{Qz}} = 0.27$  in the Fsp-saturated field. To test the effect of the roof composition (silica under- and oversaturation) on the melting rate, we varied its composition from  $X_{\text{Qz}} = 0.37$  to 0.65. This range could be viewed as silicified (quartz excess over eutectic) vs original or

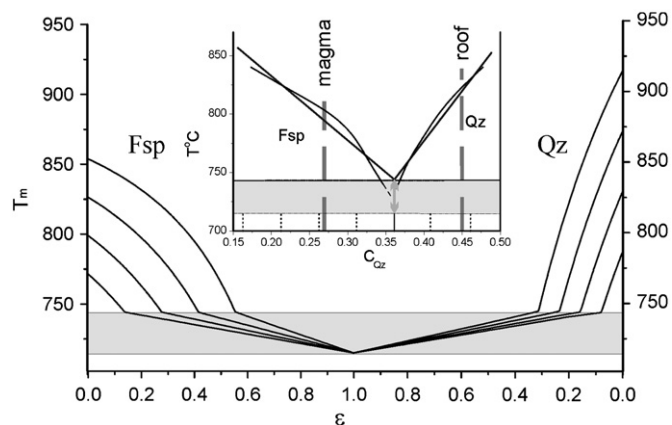


**Fig. 2.** A quartz (Qz)-feldspar (Fsp: 50% Albite+50% Orthoclase) pseudo-binary section of melting diagram Ab–Qz–Qr at  $P_{\text{H}_2\text{O}} = 1$  kbar, simplified after Tuttle and Bowen (1958), showing eutectic minima at  $\text{Qz}_{36}\text{Fsp}_{64}$ . Temperature ( $T_m$ , °C) is plotted as a function of crystal content ( $\epsilon$ ) for different bulk compositions in Qz–Fsp binary. Solid fraction increases linearly to unity with drop of  $T_m$  in the interval of the extended “eutectic” temperature (745–715 °C). Each curve in Qz and Fsp fields represents 5 wt% increment of Qz content starting from the eutectic composition. Inset shows linear approximation of cotectic lines used in present modeling. Dashed lines mark bulk compositions of magma and roof-rock used in most calculations, but some runs were done for the roof compositions in the range  $X_{\text{Qz}} = 0.37 - 0.6$ , see text.

argilitized (Fsp excess over eutectic), which is likely be present in hydrothermally altered roof-rocks.

#### 2.3.2. Viscosity, density, and Rayleigh numbers

**Viscosity.** Viscosity of the superliquidus rhyolitic melt depends on temperature, the water content, and slightly on the variations of major elements. We used a model by Holtz et al. (1999) to describe the compositional and temperature dependence of viscosity:

$$\log(\eta) = -2.8 + \frac{940 + 5598(\text{SA}/\text{HNK})^{0.3774}}{T} \quad (6)$$

where viscosity is in Pa s,  $T$  is absolute temperature, SA is atomic content of Si and Al and HNK is sum of atomic contents of hydrogen, sodium and potassium. Mean standard deviation between observed (based on experimental data set from Whittington et al., 2009) and calculated viscosities appears to be only 30%. We account for viscosity dependence on silica content by an approximate calculation of the silica increase in the Fsp–Qz binary (Fsp is taken as  $\text{Ab}_{50}\text{Or}_{50}$ ). However, most viscosity variation of subliquidus magma is due to the presence of crystals accounted for with extended Einstein viscosity relation. Viscosity of the country rocks with little or no melt is described by Power Law (see Appendix B).

**Density.** Thermal ( $\alpha_T$ ) and compositional ( $\beta_s$ ) expansion coefficients for model rhyolite have been calculated using partial molar volumes from Frederick et al. (1997), and yield typical values of  $7.3 \times 10^{-5} \text{ K}^{-1}$  and 0.05–0.1, respectively, for model rhyolite melt at  $T_o = 900$  °C,  $P_o = 1000$  bar and  $C_{\text{H}_2\text{O}} = 3$  wt% and accepting quartz and feldspar as main crystallizing phases (see Appendix B for details).

Since the density effect associated with minor changes of composition during crystallization of near-eutectic rhyolites is much less than the contribution from solid phases, in our numerical model we accepted density dependence on the temperature and crystal content only. Water has a strong influence on the density, has a large diffusion coefficient, may form bubbles, and needs special treatment that is beyond the scope of this study

that deals with water-undersaturated rhyolites, characteristic for Yellowstone, Snake River Plain, Iceland, and other intraplate environments.

$Ra_T$  and  $Ra_s$ . The gravity term in the Navier–Stokes equation can be decomposed into thermal and compositional components with correspondent nondimensional parameters:  $Ra = Ra_T + Ra_s$

$$Ra_T = \frac{\rho_0 \alpha_T \Delta T_0 g l^3}{k_T \eta_0}, \quad Ra_s = \frac{\rho_0 \beta_s g l^3}{k_T \eta_0} \quad (7)$$

With a length scale equal to the grid size, local Rayleigh numbers arise and are used as technical parameters in the numerical code. Global Rayleigh numbers with a length scale equal to the initial magma layer thickness  $H$  characterize convection vigor. Typical values of global thermal Rayleigh numbers were calculated at physical parameters from Table 1 are as follows at  $T_m = 920^\circ\text{C}$ ,  $T_o = 650^\circ\text{C}$  and  $l = H = 7.5\text{ m}$ ,  $Ra_T = 7 \times 10^6$  and compositional  $Ra_s = 1.5 \times 10^7$ . Heat effects of the phase transitions in magma have been included in the numerical model

**Table 1**  
List of abbreviations used in the paper.

Linear coordinates: $x, y$	
Linear sizes	
$l$ —thickness of the magma layer	10–100 m
$l_o$ —linear scale for computational grid varying in the range (0.5–1) $l_o$	0.25 m
Time $t$	
$t_o$ —time scale $l_o^2/k_T$	1.23 days
Pressure $P$	
$P_o$ —ambient pressure	1 bar
Rate $u$	
$u_i = (u_x, u_y)$ convection rate	
$u_m$ melting rate	
$u_o = k_T/l_o$ velocity scale	74.9 $\text{ma}^{-1}$
$u_m^v$ lower threshold melting rate	2 $\text{ma}^{-1}$
Temperature $T$ of	
$T_m$ magma	800–940
$T_s$ solidification	730
$T_o$ initial roof	200–700
Acceleration due to gravity, $g$	
Heat transfer coefficient, $\lambda = c_p \rho k_T$	2.0 $\text{W/m/k}$
Thermal diffusivity coefficient, $k_T$	0.6e–06 $\text{m}^2/\text{s}$
Heat capacity $c_p$	1.34 $\text{kJ}/(\text{kg K})$   0.32 $\text{cal/g}^\circ\text{C}$
Enthalpy $H$	
Heat of fusion $\Delta H_m$	213.5 $\text{kJ/kg}$   51 $\text{cal/g}$
Density $\rho$	
$\rho_0$	2500 $\text{kg/m}^3$
$\alpha_l, \beta_l$ coefficients of melt density ( $T, P$ ) series expansion (Eq. (14))	
$\alpha_T$ thermal expansion coefficient	6.6e–05 $\text{K}^{-1}$
$\Delta \rho_{T,o} = \rho_0 \alpha_T (T_s - T_o)$ thermal density difference	
$\Delta \rho_{s,o} = \rho_s - \rho_l$ phase density contrast	200 $\text{kg/m}^3$
$V$ partial molar volume (Eq. (15))	
Quartz weight concentration $C$	
fraction	
$\epsilon$ ( $\epsilon_l, \epsilon_s, \epsilon_g$ )	
volume fraction of phase: l—liquid, s—solid, g—glass	
Magma viscosity $\eta(T, C)$	
$\eta_o$ viscosity scale	57000 Pa s
Calculated at $T = 860^\circ\text{C}$ , $C_{qz} = 0.3611$	
Strain rate $\dot{\epsilon}$ ( $\dot{\epsilon}_{II}$ —second invariant of the strain rate tensor)	
Dynamic power law parameters (Eq. (11)): a, b, m	
Convective heat flux $q_{conv}$ ( $\text{W/m}^2$ )	
Grid nondimensional Rayleigh number	
Phase composition related $-Ra_s$	1050
Thermal $-Ra_T$	variable
Nondimensional Stefan number $Ste = \Delta H_m / c_p \Delta T$ calculated with case specific $\Delta T$	

by specifying an effective heat capacity coefficient (see Eq. (5)) calculated for particular  $\partial \epsilon_s(X_o, T) / \partial T$ , defined by the phase diagram approximation described above, and fixed  $\Delta H_m = 231\text{ kJ/kg}$ .

### 3. Results of numerical runs

We have performed 250 numerical runs under different initial and boundary conditions to explore convective patterns and melting rates, robustly “map” melting regimes and their characteristics (e.g., Fig. 3), as well as outline conditions at which the process changes to the catastrophic roof failure due to thermo-elastic crashing. Several series of the relatively short runs were aimed to estimate the initial mid-run melting rates in the wide range of  $T_o$  and  $T_m$  (Fig. 3), and several long runs were aimed to demonstrate how melting processes and rates are evolving with time, and what qualitative processes are occurring in these long runs. Results of these numerical experiments are presented in Figs. 4–7, movies in avi format are available in the Appendix, and results are discussed below.

#### 3.1. General observations

Upon emplacement of the magma sill, but before the onset of convection, solid roof contacts are heated conductively, while magma conductively cools and crystallizes, forming a transient crystal + melt zone at the contact. As the temperature of the roof-rock contact rises above the eutectic ( $715^\circ\text{C}$  in our simulation), partial melt appears in the roof further extending the crystal + melt zone upwards. This transient process of formation of the unstable boundary layer is reflected as a delay time in the plot of Fig. 4a. After this initial time, the boundary layer becomes gravitationally unstable and develops a set of descending cold thermal and compositional plumes, and this process evolves

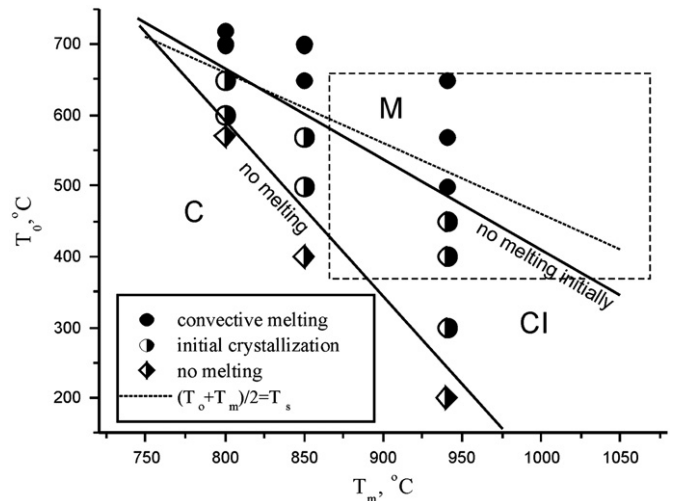


**Fig. 3.** Summary diagram of melting regimes based on results of numerical runs with thin (5–7.5 m) rhyolitic sills with initial temperature  $T_m$ , intruded into the rhyolitic roof-rocks with temperature  $T_o$  (Fig. 1). Symbols describe observed regimes of experiments: M, melting of the roof starts from the beginning; CI, initial conductive solidification of intruded magma, followed by roof melting, after initiation of convection; C, crystallization without melting during all run. Dotted line satisfies self-similar solution in conductive regime  $(T_o + T_m)/2 = T_s$  and separates fields of magma solidification with and without roof melting. Dashed rectangle displays range of characteristic temperatures  $T_m$  for rhyolites from the Snake River Plain (Bindeman et al., 2001; Nash et al., 2006; Watts et al., 2011), and possible ranges of roof temperatures,  $T_o$  of rhyolites buried at different depths. Note that results of the present simulations of convective melting permit melting of much colder, 300–400  $^\circ\text{C}$  roofs than is achievable in conductive regime (dotted line).

exponentially through time, quickly reaching near-steady state convection. Mid-run convection is chaotic, and we observe that the convection rates are fairly rapid, reaching up to 20 m per day, (with peak rates up to 30 m/day at the beginning of convection) but with average rates of  $\sim 10$  m/day (see Fig. 4b for horizontally averaged velocities). Whereas spatially averaged over the whole computation domain (including rocks) rates are several times smaller (Fig. 4a). We also find that convective rates depend on the temperature difference  $\Delta T = T_m - T_s$  but do not depend on the initial roof temperature, and only weakly on the magma temperature (Fig. 4). For purely thermal convection, the rate of

convection is proportional to  $\Delta T^{2/3}$  (Turcotte and Shubert, 2002). In our experiments variation is smaller (less than 30%) since for the lower magma temperatures convection is essentially compositional with larger than thermal density difference.

Variation of horizontally averaged convection rates are plotted in Fig. 4b as a function of magma temperature, from central convective cores to the rigid and cold boundary layers (Suppl. material). Convective rates rapidly diminish by more than 2 orders of magnitude from the cores toward the viscous boundary layer, where convection practically stops at  $T \approx 735\text{--}745$  °C, i.e. at the beginning of the extended crystallization in the eutectic

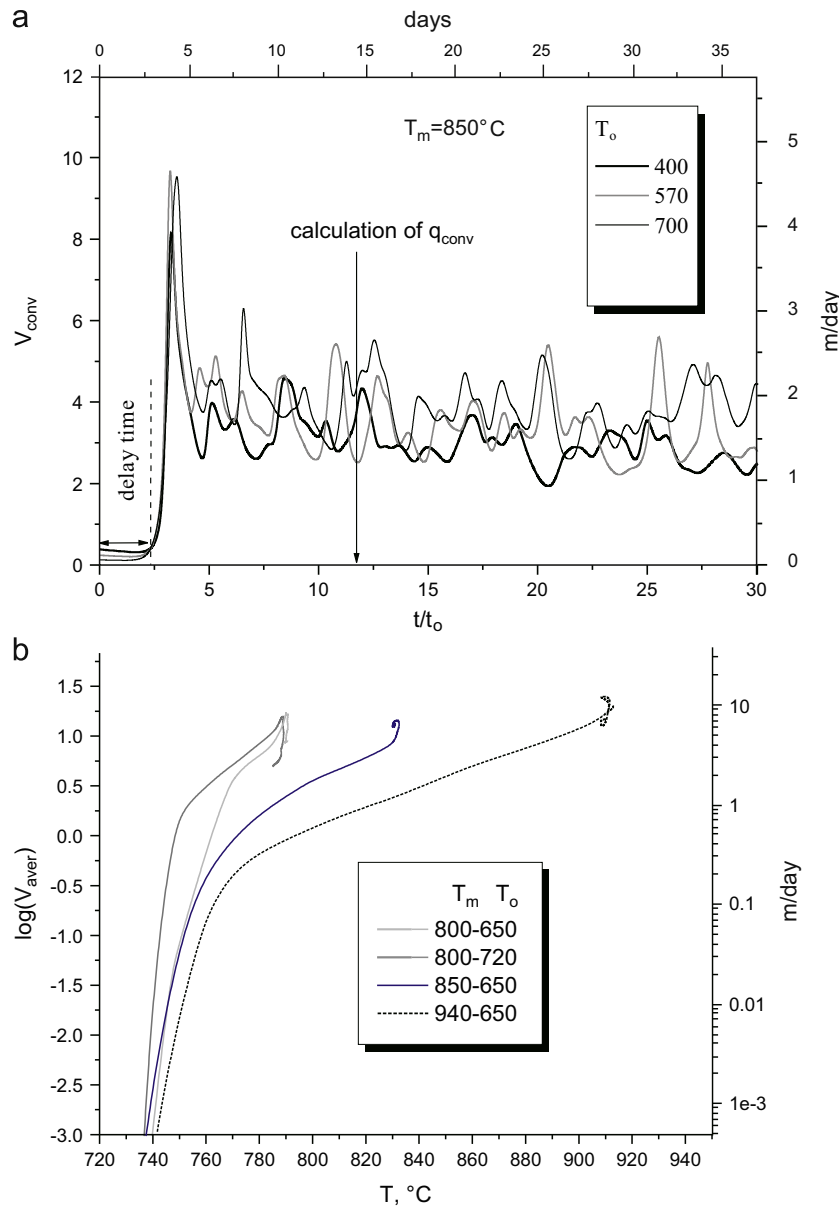


**Fig. 4.** Convective velocities (nondimensional and dimensional) as a function of time and temperatures  $T_m$  and  $T_o$ . (a) Spatially averaged convective velocities as a function of time for magma with  $T_m = 850$  °C and roof-rocks with different temperatures shown on the inset. Notice that the average convection velocities in these chaotically convecting viscous rhyolitic magmas are on the order of meters per day, but the maximum velocities are ca 10 times faster, e.g., meters per hour. Also notice that the average convective velocities stay constant for a long time into the melting run, and do not significantly depend on roof-rock temperatures. Arrow indicates time step used to calculate the temperature space derivate (Fig. 6c). The delay with initiation of convection is due to the time necessary to form cold two-phase boundary layer (e.g., Fig. 5). (b) Vertical profile of horizontally averaged convective velocities in the middle of the melting run (6000th time step) for different temperatures  $T_m$  of intruded magmas and temperatures of the roof-rock  $T_o$ . This graph can be visualized as vertical cross sections through the system as is shown in Fig. 5, with “fast” and hot convecting core and “slow” and cold boundary layers. Rapid convective velocity decrease toward the cold boundary layer is explained by increase in viscosity due to the increase in crystallinity and decrease in temperature; rapid collapse of convective velocities to vanishingly small rates occurs in the near-eutectic temperature interval 740–760 °C where there is nearly isothermal increase in crystal content. Also notice that the lower and more viscous part of the boundary layer is capable of being entrained into convection at the lower  $T_m$ , explained by the lesser viscosity contrast.

temperature interval of 715–744 °C. This result is important and it adequately describes the dynamics of transition from stagnation to rapid convection in natural silicic magma systems with a eutectic. Upon onset of convection, convectively stirred cores are characterized by narrow intervals of velocity and temperature variations (Fig. 4b), and the average convection rates in the sill's core only slowly decrease with time, in response to gradual decrease in  $T_m$ .

Depending on the starting roof and magma temperatures  $T_o$  and  $T_m$ , position of the magma/roof interface may initially migrate upward into the roof (roof melting, regime M, Fig. 3) or downward (magma solidification without roof melting, regime CI, Fig. 3). Since in the initial moment of heat exchange phase transition occurs through pure conduction, it is straightforward to delineate these two regimes via the self-similar solution of the correspondent Stefan problem: when roof and underplating magma have identical melting diagrams, this boundary in  $[T_o, T_m]$  space is defined simply by condition  $(T_o + T_m)/2 = T_s$ .

In Fig. 3 we present starting conditions and regimes of numerical experiments performed using a rhyolitic phase diagram (Tuttle and Bowen, 1958) with crystallization intervals as shown in Fig. 2. Perhaps the most important observation resulting from consideration of real phase diagram is that melting can occur significantly below the line defined by  $(T_o + T_m)/2 = T_s$ . In particular, we observe that 850 °C underplating magma can melt 475 °C roof-rock, after a brief period of crystallization. Fig. 3 also shows typical temperature ranges for Yellowstone magmas, and suggests that even 'cold' roof-rocks of 450–550 °C are capable of being remelted.

### 3.2. Physical processes observed in numerical runs

Convection in runs with different  $T_m$  and  $T_o$  and proportions of quartz in the roof are characterized by relatively similar convective patterns (see Fig. 5a–d for compositional and thermal fields, and AVI movies of two long-term runs are available in the supplementary materials). The following is observed:

- (1) Convection has mixed compositional (density variation controlled by crystal content) and thermal character.
- (2) Convective motion is initiated by descending plumes near the partially molten boundary layer in the roof (Fig. 5), detachment of plumes from the roof proceeds at the temperature near the upper limit of the eutectic interval at 745 °C.
- (3) Horizontal spacing of plumes is only 1.5–2 m in rhyolites modeled in this work. The outer part of the individual thermal plume stem is composed of the cooled magma. A sharpening downwards shape of protrusions (ridges) of the roof material reflects a downward increase of the plume detachment rate.
- (4) Descending plumes that are rooted in the material with high viscosity have low horizontal mobility. However, episodically pairs of plumes interact and coalesce during descent, mixing their crystal contents.
- (5) Melting is accompanied by "erosion" of the roof by convective currents, in addition to true melting. By erosion we mean melting happening not by advancing of the flat "Stefan" front, but rather by protrusions along the wavy boundary (Fig. 5) and involving assimilation of the detached pieces of the roof magma. What we observe in our numerical experiments is reminiscent of qualitatively described "reactive bulk assimilation" processes (Dungan and Davidson, 2004; Beard et al., 2005), in which roof-rock loses cohesiveness upon small degrees of melting, supplying rocks chunks and "crystal cargo" into the underlying convecting magma.
- (6) Variation of the composition of the roof-rock (% of SiO<sub>2</sub>, quartz under- or over- saturation) has very small impact on the convective regimes.

- (7) In several experiments we modeled the behavior of inhomogeneous roof-rock with blocks of higher melting temperatures (see [avi movie in the supplementary materials](#)). These roof-rock blocks may represent intrinsic inhomogeneities with respect to their solidus temperature present in any roof. The melting front bypasses blocks, causing them to mechanically collapse, which temporarily increases convection rates. Furthermore the scar left in the roof-rock after the block detachment gets invaded by fresh hot magma, creating steep temperature gradients. Thus, if the roof-rock is inhomogeneous and contains fragments with higher melting temperatures, the gravitational energy released upon their fall will accelerate assimilation.
- (8) When the temperature of the well-mixed convective core is above the liquidus  $T_l$  for a given quartz content ( $X_{Qz}$ ), no crystals survive inside in our model. Therefore crystals contribute to the density contrast only in the uppermost part of the plumes since they are soon dissolved downward in the equilibrium approach used in this study. In natural systems, crystals dissolve much more slowly than convection, as dissolution is controlled by slow element diffusion through the melt (e.g., Zhang et al., 1989). The accelerating effect of the crystal load is better expressed in our runs with  $T_m$  close to the liquidus temperature, as is shown below (see Fig. 7).

### 3.3. Temperature profiles

Horizontally averaged temperature distributions (Fig. 6a) exhibit asymmetry as convective melting of the roof proceeds and the temperature of the convecting core falls, whereas the roof maintains approximately the same temperature as the conductive front moves with the melting boundary. In the simplified theoretical models (e.g., Huppert and Sparks, 1988), phase transition takes place at a fixed temperature, while in our numerical model a specific temperature interval is used depicting realistic behavior of near-eutectic silicic systems. As a result, localization of the maximum heat consumption at melting is expressed as the second derivative of temperature  $d^2T/dy^2$  as a function of temperature (Fig. 6b). The maximum heat consumption takes place around  $T \approx 730$  °C, in the middle of the extended eutectic interval.

We recalculate evolution of the  $T=750$  °C isotherm on the temperature profile  $T(y)$  at the melt–solid interface in coordinates moving with the melting front. In Fig. 6c two numerical distributions are plotted along with a theoretically calculated steady-state distribution. Theoretical values are found as solutions (calculated with Maple 9.5) of the 1D heat conduction PDE in the coordinates moving with constant rate  $u_m$ . In non-dimensional units this equation reads:

$$\frac{\partial T}{\partial t} = \bar{u}_m \frac{\partial T}{\partial x} + \frac{\partial^2 T}{\partial x^2} \quad T(0, x) = 0; \quad T(t, \infty) = 0; \quad T(t, 0) = 1 \quad (8)$$

Small differences between the numerical and theoretical values can be noted. We observe in Fig. 6c that in short experiments with 5 m sills thicknesses temperature distribution in the roof is far from being at steady-state, implying small thermal evolution time. It follows that in the parametric models of melting by thin sills (with thickness less than ca 30–40 m), transient thermal distribution ahead of the melting front should be used, instead of the steady-state approximation accepted in Huppert and Sparks (1988). Transient temperature distributions have gradients in the melting front that are 1.5–2 times larger than stationary ones (Fig. 6c), which is important for estimating melting efficiency (Section 4.2).

Furthermore, high thermal gradients may cause extreme thermoelastic stresses leading to mechanical failure of the rocks

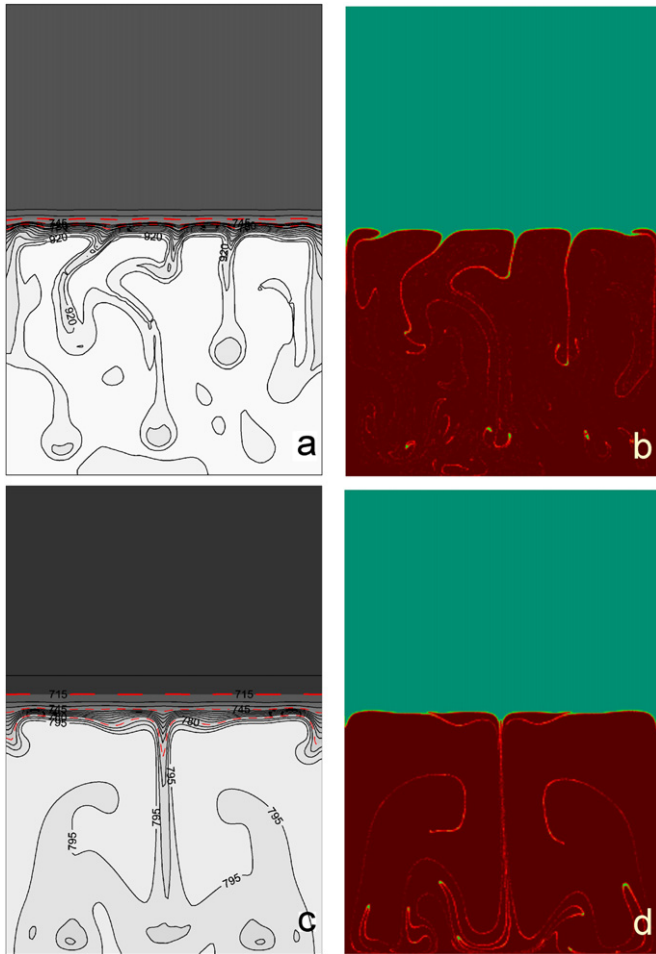


**Fig. 5.** Screenshots of numerical runs, showing temperature (a,c) and composition (b,d) distributions, see supplementary materials for avi movies. Resolution is  $120 \times 180$  (initial  $120 \times 100$  or  $10 \times 8.3$  m for magma domain). (a,b) Run with  $T_m=940$  °C,  $T_o=650$  °C, at  $t=2.3$  days, (c,d) run with  $T_m=800$  °C,  $T_o=700$  °C, at  $t=2.3$  days. Two phase region is contoured by isotherms 715 and 780 °C (dashed lines). Color variation from the cyan to dark red in compositional plots (b,d) corresponds to the relative content of the upper layer ( $X_{O_2}=0.45$ ) in the lower one. Jets depict plumes descending from the roof. Notice here and in avi movies chaotic plume behavior, their interaction, and redistribution of roof material (see text for discussion).

ahead of the melting front. Low viscosity of the heated rocks requires accounting for viscous relaxation reducing the level of stresses. Solution of the simplified version of the moving boundary problem in the viscoelastic halfspace suggests that at the threshold melting rate of about 10 m/yr, thermal gradients may create conditions for thermoelastic crushing of the roof and facilitate the assimilation process. The feedback between melting rate and thermoelastic crushing is important and is addressed in Section 4.3.

### 3.4. Melting rates

Melting rates that we observe in our runs range from meters per year to meters per month. Position of the melting front shifts steadily with time into the roof for the melting regime M (Figs. 3 and 6a). In the initial crystallization regime CI, roof melting proceeds after a longer delay. In long runs, all melting processes decelerate due to cooling and crystallization of the magma sill. Thus, to characterize the melting rate we used time after the onset of convection and before considerable nonlinearity of propagation. Heat transfer in the roof is of primary importance

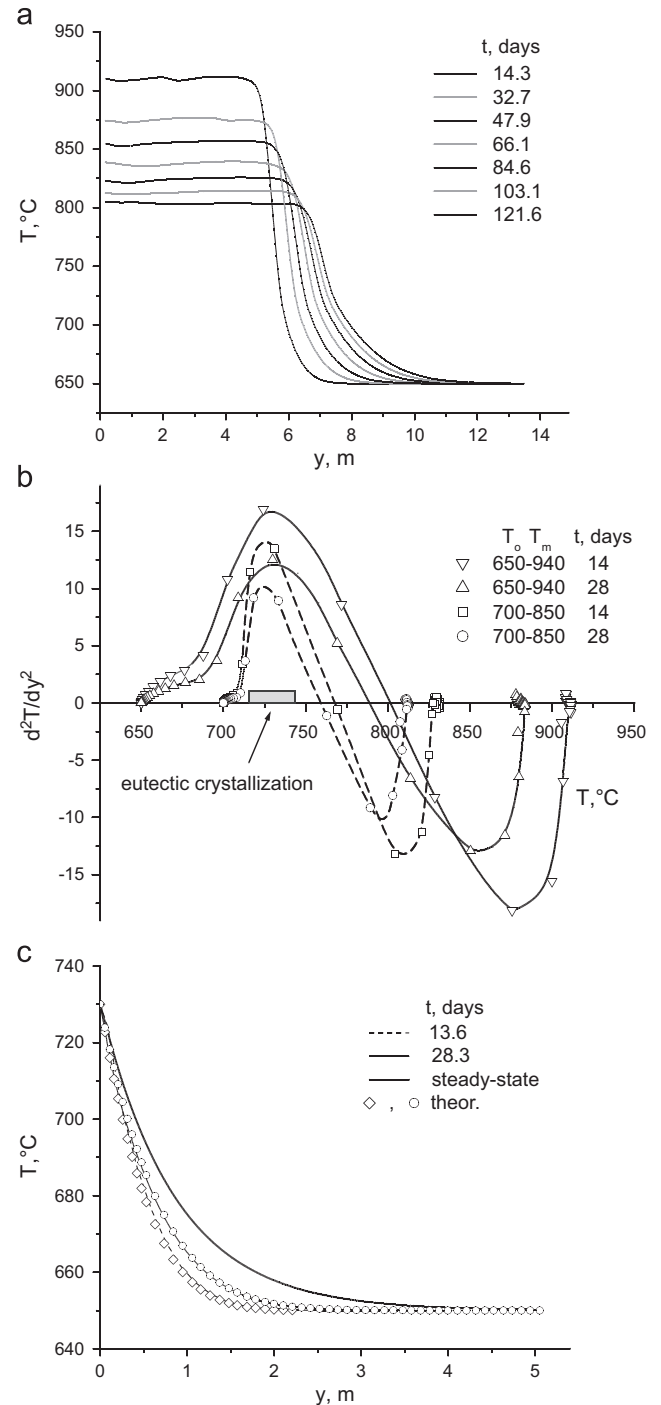


**Fig. 6.** Horizontally averaged temperature distributions for a 5 m sill with  $T_m=940$  °C, intruded into the roof-rocks with  $T_o=650$  °C. (a) Long run demonstrating convective magma cooling by melting and propagation of the upper boundary layer; (b) localization of the heat sink (displayed by  $d^2T/dy^2$ ) on the horizontally averaged  $T(y)$  distribution at the specified parameters. Note that the maximum expected heat consumption coincides with the temperature range of eutectic crystallization (gray rectangle). (c) Temperature profile (in the coordinates moving with  $u_m$ ) in the solid roof at the melting boundary through time. Thick line depicts steady-state exponential distribution at nondimensional mid-run melting rate  $u_m=0.1942$ ; symbols depict theoretical solutions of the conduction moving boundary problem (see text for details). Notice little change in  $dT/dz$  profile through time, suggesting that high convective heat transfer and melting rates will persist throughout the course of melting, keeping temperature boundary layer sharp.

as the melting rate is determined by the values of the convective heat flux and temperature gradient in the roof at the front position. Average convective melting rates (in m/yr) with

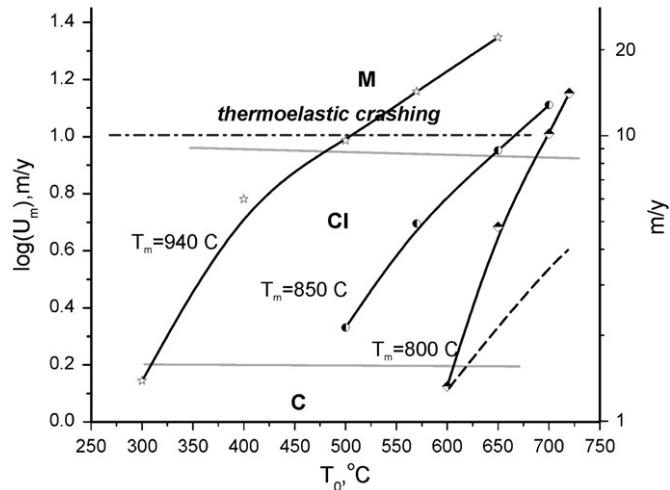


**Fig. 7.** Initial melting rates for numerical runs at different  $T_o$  and  $T_m$ . Gray lines delineate parametric fields of different melting regimes (see caption to Fig. 3 for explanation). With increase in melting rates to higher than  $\sim 10$  m/yr, the strong temperature gradient (of the order  $100^\circ\text{C}/\text{m}$ ) ahead of the melting front may cause thermoelastic crushing of the roof-rocks (labeled by dashed line), causing chunks of the roof mechanically collapse into the sill, see Section 4.3 for discussion. Numerical melting rates have been compared with semi-parametric estimates obtained with modified Huppert and Sparks (1988) model. Both approaches appear to get close results as can be seen in Appendix D.

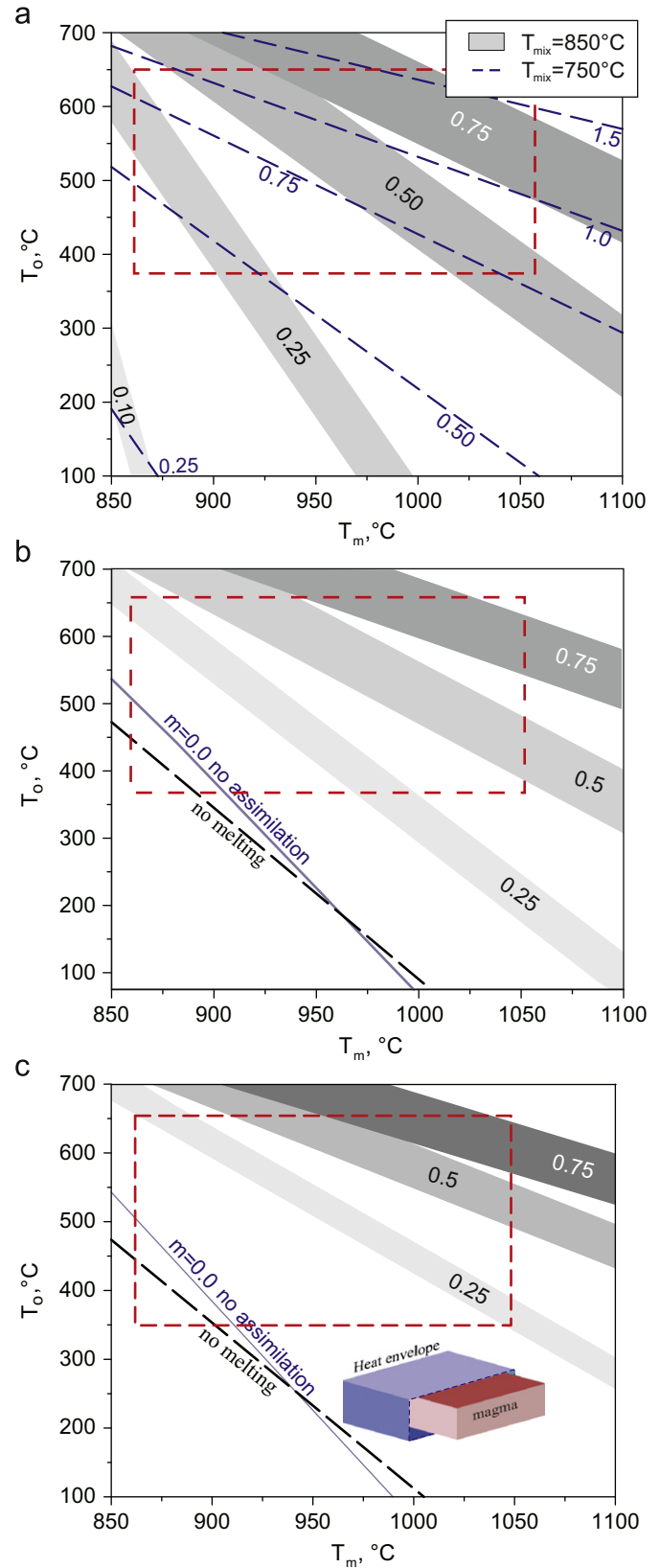
parameter values from Table 1 are displayed in Fig. 7. Three curves show strong dependence of melting rate on the initial magma temperatures ( $T_m$ ) and roof-rock temperature  $T_o$ . However, the transition boundary between M (melting) and CI (crystallization initially, then melting) regimes stays approximately constant  $9$  m/yr for different  $T_o$ . At  $T_m = 800^\circ\text{C}$  the melting rate rises much faster with increasing  $T_o$  than for higher initial magma temperatures. This acceleration of melting is explained by faster convection resulting from the larger contribution of crystals existing in the whole volume to density contrasts while at high  $T_m$  crystals are present only the uppermost part of the boundary layer as shown below.

**4. Discussion**

Our numerical modeling results demonstrate that shallow melting of buried rhyolitic rocks by hot or superheated rhyolites

**Fig. 8.** Amount of assimilated subsolidus roof-rock,  $\gamma$ , expressed as fraction to the original volume of underplated magma for different values of thickness of magma layer, that achieves  $T_{\text{mix}} = 850^\circ\text{C}$  with liquid fraction  $e_l = 0.6$  (dark fields) and  $T_{\text{mix}} = 750^\circ\text{C}$  dashed lines. Underplating magma has temperature  $T_m$  and is crystal free, roof-rock has temperature  $T_o$ . Value of  $\gamma$  is constant in each filled domain, but the proportion of glass  $e_g$  in the assimilated roof-rock varies from 0 (less assimilation, lower boundary) to 0.7 (more assimilation, upper boundary). For  $T_{\text{mix}} = 750^\circ\text{C}$  we set  $e_g = 0$ . As glass stores latent heat of crystallization, its release upon heating extends field of the constant  $\gamma$  to the colder roof ( $T_o$  lower on  $100^\circ\text{C}$  on average). Dotted rectangle displays range of  $T_m$  temperatures characteristic for rhyolites from the Snake River Plain (see Fig. 9), and possible ranges of roof temperatures,  $T_o$  (see Fig. 3). (a) Amounts of assimilation by a  $150$  m sill. Notice that significant variations in the amounts of assimilation are possible. (b) Amounts of assimilation by a  $30$  m sill with melting rate reducing exponentially with time from  $12$  to  $2$  m/yr (see supplementary materials for explanations). Continuous line for  $\gamma = 0$  depicts lowest possible  $T_o$  and  $T_m$  capable of producing  $T_{\text{mix}} = 850^\circ\text{C}$  with liquid fraction  $e_l > 0.6$ . Boundary of the beginning of melting for  $h = 5\text{--}7.5$  m sill based on numerical calculations is shown with thick dashed line for comparison as in Fig. 3. (c) Amount of assimilation by a  $30$  m sill at the uniformly slow melting rate  $u_m = 2$  m/yr. In the insert “brick” represents magma surrounded by envelope of the conductively heated rocks. Heating without melting is countered as  $Q_{\text{loss}}$  in Eq. (11) at the closure of convective melting.

coming from below can be a rapid process with linear melting rates of up to  $10$  m/yr. We consider the implications of these fast melting processes for magma production rates in studied calderas of Yellowstone and the Snake River Plain. We also provide simple



estimates of the attainable amounts of assimilation and apply these results to thicker sills and larger magma chambers.

#### 4.1. Melt productivity and degrees of assimilation

Maximum productivity of melting and assimilation can be estimated by a simple energy balance. The enthalpy surplus of the underplating magma per unit mass is

$$\Delta H_1 = (T_m - T_o)c_p + \Delta H_m \quad (9a)$$

where  $T_o$  is the reference temperature. Upon assimilation of  $m$  weight units of the roof-rocks, the final heat balance is

$$(T_m - T_o)c_p + \Delta H_m - Q_{loss} = (1 + m)(c_p(T_{mix} - T_o) + \Delta H_m \varepsilon_l) \quad (9b)$$

where  $\varepsilon_l$  and  $T_{mix}$  are the melt fraction and temperature in the final mixture, respectively. We obtain a relationship between the temperature of assimilation product  $T_{mix}$  and mass fraction of the assimilant added  $m$ , calculated for  $\varepsilon_l = 0.6$  and other parameter values from Table 1 (Fig. 8a). Without heat loss ( $Q_{loss} = 0$ ), substantial amounts of assimilation of silicic roof-rock ( $m$ ) of many tens of percent can be achieved by hotter rhyolites. For example, a hot rhyolite with  $T_m = 1050$  °C can assimilate 50–60% of the relatively cold, 400 °C roof-rock. While  $Q_{loss} = 0$  condition is obviously not realistic, below in Section 4.2 we discuss realistic heat losses given the very short melting timescales involved. To achieve even more significant degrees of assimilation ( $m > 0.5$ ), approaching that of bulk melting, which are required for some rhyolites with exclusively xenocrystic zircon and quartz populations (e.g., Canyon and Dunraven Road flows of Yellowstone, Bindeman et al., 2008), and to generate hotter low-silica rhyolites (with  $T_{mix}$  close to 900–1000 °C, e.g., Nash et al., 2006) that occur in the Central Snake River Plain, either a repeated process raising  $T_o$  to near-solidus (650–750 °C) temperatures (Fig. 1) and/or their generation by hotter magmas with high  $T_m$  are required.

Here, we also draw special attention to one important aspect related to the remelting process of rapidly-buried, glassy rhyolitic predecessors. If glass fraction in assimilated rock is  $\varepsilon_g$ , the latent heat of crystallization from glass will add an additional  $m\varepsilon_g\Delta H_m$  to the starting enthalpy:

$$(T_m - T_o)c_p + \Delta H_m + \varepsilon_g m \Delta H_m - Q_{loss} = (1 + m)(c_p(T_{mix} - T_o) + \Delta H_m \varepsilon_l) \quad (10)$$

Thermodynamic estimates for assimilation of glassy rhyolites with  $\varepsilon_g = 0.7$  comprise the upper limit for shaded areas with constant  $m$  in Fig. 8a. An increase in the assimilation degree of glassy rhyolites becomes increasingly important for higher  $T_o$  and  $T_m$ .

#### 4.2. Heat losses and the simplest estimate of the melting and assimilation efficiency

Long-term crustal melting efficiency (e.g., Dufek and Bergantz, 2005) is a function of the proportion of dissipated thermal energy, which in turn is a function of the complex physical state of the surrounding rocks, and may involve hydrothermal refrigeration for example. While current models disfavor upper crustal melting, our work shows that melting efficiencies could be much higher than previously advocated, and approach 70–85%, if melting rates are ‘rapid enough’. We estimate the  $Q_{loss}$  term in Eq. (11) in Appendix C and explore achievable degree of assimilation as a function of the sill’s thickness  $h$ . By setting temperatures  $T_o$  and  $T_m$ , protolith glass content  $\varepsilon_g$ , thickness of the magma layer  $h$ , mixture temperature  $T_{mix}$  and melt content in product of assimilation  $\varepsilon_l$  we determine the assimilation degree  $m$ . At the initial heating of the surrounding rocks thin sills reach  $T = T_{mix} = 850$  °C and solid fraction 0.4 when convection is locked and magma cannot assimilate roof material so that “zero-assimilation”

boundary can be defined in our simplified model for small  $h$ . In Fig. 8b and c we present results of calculations for layers with thickness  $h = 30$  m and compare them with results of numerical runs done for smaller 5–7.5 m sills. One can note that the boundary at the beginning of numerical melting closely corresponds to a ‘zero assimilation’ boundary in heat balance calculations. Calculations also show that a ~100 m sill nearly reaches assimilation degrees defined by thermodynamic enthalpy contents (Fig. 8a) with minimum relative heat dissipation.

#### 4.3. Conditions for catastrophic roof failure and collapse

The estimated efficiency of the melting process can be dramatically increased (and time required for bulk assimilation decrease), if there is a mechanical roof failure, resulting from roof block foundering. This may be caused by disaggregation of a partially molten roof but we outline an additional process—chipping of the roof by thermoelastic stress. The order of magnitude of mechanical stresses arising at the melting front can be estimated as follows. In the boundary layer ahead of the melting front the temperature varies from  $T_o$  to  $T_m$ , therefore the magnitude of the deviatoric component of thermoelastic stress is determined by applying elastic constitutive and equilibrium equations:

$$s_{xx}(y) = -\frac{4\mu\alpha_T(T(y) - T_o)(\lambda + \mu)}{\lambda + 2\mu} \quad (11)$$

where  $\lambda$  and  $\mu$  are Lamé constants and  $\alpha_T$  is the coefficient of thermal expansion (Table 1). In doing so, we only considered the possibility of vertical movements above horizontally extended sill. As can be seen from Eq. (11), elastic thermal stresses are the greatest at the melting front, however, when  $T$  approaches  $T_m$ , the thermal stress experiences fast viscous relaxation and completely vanishes at  $T = T_m$ .

Next, using constant effective viscosity for the rocks with Maxwell viscoelastic rheology in the thermal aureole (as is accepted in Newman et al., 2006 for the Long Valley Caldera), we analytically solve the correspondent moving melting boundary problem and find a value of steady-state  $s_{xx}$  (to be published elsewhere). The exact solution appears to be close to the scaling estimate presented below. Near the steady state, the Deborah number (the ratio of Maxwell relaxation time  $\eta^*/\mu$  to observation time) becomes negligibly small, and the solution should depend on this effective viscosity instead of the Lamé constants. The only combination of the involved physical parameters ( $k_T$ ,  $\eta^*$ ,  $u_m$ ,  $\alpha_T$ ,  $\Delta T$ , Table 1) with the dimension of stress is

$$\sigma_T = \frac{\Delta T \alpha_T \eta^* u_m^2}{k_T} \quad (12)$$

At a melting rate of  $u_m = 11$  m/yr, and  $\eta^* = 5 \times 10^{16}$  Pas as in (Newman et al., 2006),  $\alpha_T = 5 \times 10^{-5}$  K<sup>-1</sup>,  $\Delta T = 200$  °C we obtain value of  $\sigma_T = 100$  MPa. This value the thermoelastic stress achieved due to fast melting exceeds the shear-strength of roof-rocks leading to their thermoelastic chipping into the convective magma.

The outlined process is self-sustaining, because there is a feedback between this “mechanical” fragmentation of the roof with block detachment that maintains steep temperature gradient, and melting rate. At fast melting rates  $> \sim 10$  m/yr, such coupling may lead to the thermoelastic chipping off or “mechanical burning of” the upper roof boundary.

#### 4.4. Applications to Yellowstone, Snake River Plain calderas, and early Earth environments

The genesis of silicic magmas is obviously a poly-genetic and multi-staged process (e.g., McCurry et al., 2008; Streck and

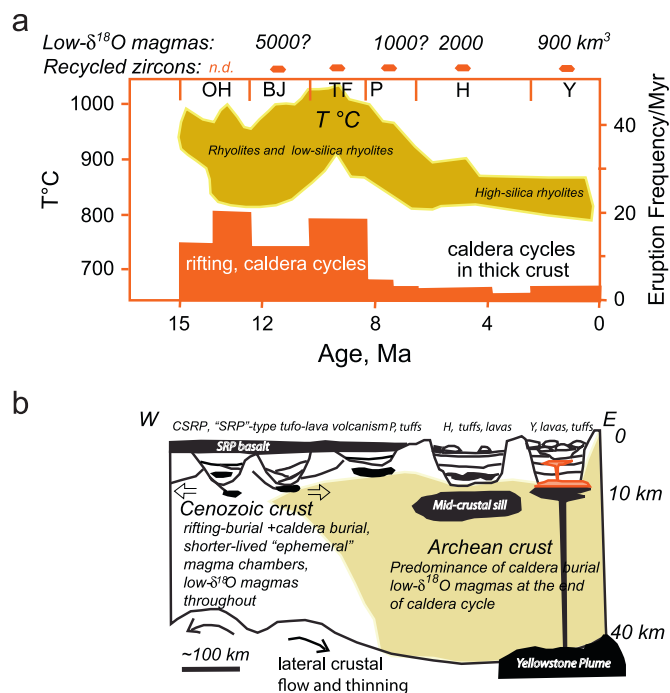


**Fig. 9.** Magmatic remelting processes along the Yellowstone hotspot calderas forming the Snake River Plain (SRP). Notice that low- $\delta^{18}\text{O}$  rhyolites with recycled, diverse in  $\delta^{18}\text{O}$  zircons are now found in all studied caldera centers along SRP (see Watts et al., 2011, and our unpublished data). Diversity of  $\delta^{18}\text{O}$  signifies remelting of variably hydrothermally altered buried rhyolites. (a) Temperature and eruption frequencies of rhyolitic magmas along the SRP (modified after Nash et al. (2006)). Shown caldera cluster centers, west to east are: OH—Owyhee-Humboldt, BJ—Brunneau-Jarbidge, TF—Twin Falls, P—Picaboo, H—Heise, Y—Yellowstone. (b) Crustal cross-section along the SRP showing nested calderas, buried silicic tuffs and lavas, basalt-driven remelting processes. We suggest that caldera-burial dominates volcanism in the thicker Archean crust in the eastern SRP. Thinner and more mafic crust in the west is undergoing Basin and Range extension and lateral lower crustal escape flow near Moho. These processes lead to direct remelting by hotter and more mafic magmas, explaining hotter temperatures and lower-silica contents. Extent of the Archean crust and magma-tectonic processes are from Leeman et al. (1992), McCurry and Rogers (2009), and geophysical mid-crustal basic sill is from Peng and Humphreys (1998). We suggest that the crustal “cannibalization” processes that we model in this paper lead to basic-silicic stratification of the middle-upper crust along the SRP, and does not leave behind granitic batholiths in the wake of the plume.

Grunder, 2008; Christiansen and McCurry, 2008; Whitaker et al., 2008), but intraplate A-type magmas are all notoriously hot and dry, in contrast to mush-extracted near-solidus cold melts elsewhere (see Bachmann and Bergantz, 2004 for review of the “mush” literature). The mechanism advocated in this work allows for relatively quick ( $10^3$ – $10^4$  yr) formation of large-volume, highly fractionated, high- and low-silica rhyolitic magma chambers in the upper crust and do not rely on extraction from a preexisting long-lived granitic mush in the lower-middle crust. In our model, the very first normal  $\delta^{18}\text{O}$  rhyolites at the beginning of each caldera cycle are produced (more slowly) by a combination of basaltic magma differentiation (e.g., McCurry et al., 2008) and crustal melting (e.g., Streck and Grunder, 2008), yielding bimodal basalt-rhyolite sequences. Fig. 9 demonstrates transition from rift to caldera burial processes characteristic from W to E Snake River Plain, neither environment is underlain by geophysical batholiths, but rather by “basaltic sills” (Peng and Humphreys, 1998). We show in our calculations that at high but subsolidus  $T_0$ , even small portions of hot rhyolites may melt and assimilate large amounts of roof material. The cooling and evolution time of small batches of magma is short, compared to dissolution time of zircon and even quartz crystals (especially when thermoelastic crushing will reduce assimilation time). While applying our results to

different cases of shallow rhyolite magma genesis, we need to test our model with well-established observations. More specifically isotopic and geochronologic data unambiguously support a high proportion ( $> 0.3$ – $0.4$ ) of hydrothermally altered roof-rocks and associated crystal cargo in late-stage low- $\delta^{18}\text{O}$  rhyolites of caldera centers of the Snake River Plain (Bindeman et al., 2006, 2008; Watts et al., 2011) or rift zones of Iceland (Carley et al., 2011; Bindeman et al., 2012). Furthermore, crystal size distributions (CSD) of zircons and quartz (Simakin and Bindeman, 2008), and age patterns of inherited zircon (e.g., Miller and Wooden, 2004; Carley et al., 2011), only require one to three episodes of moderate remelting without reaching full dissolution. A massive roof collapse into a pool of underlying magma (thermoelastic or block failure regimes) may serve as a mechanism of “bulk assimilation”. As a result, inherited and progressively annealed initial “crystal cargo” will get distributed by convection and can mix with the newly crystallized assemblage leading to rather complex “pheno”+“ante”+ “xeno”-cryst and zircon crystal populations (Bacon and Lowenstern, 2005; Bindeman et al., 2008). Their age-frequency plots span anywhere from multimodal “xenocrystic” (e.g., Bindeman et al., 2001), to long-tail antecrystic (e.g., Reid, 2003), to short-tail “phenocrystic”, signifying variable residence-recrystallization times. Temperature estimates from these hot recycled rhyolites (Nash et al., 2006; Watts et al., 2011) can be similarly diverse, reflecting complexity of the process, and in many cases they are crystallization-minimal temperatures, not maximum magma temperatures.

We suggest that caldera processes, rift processes, and early-Earth ‘suck’duction burial processes, aided by hydrothermal alteration and silicification of the roof-rock, will lead to the effective burial of rhyolites in the upper crust. The remelting process described in this paper leads to progressive distillation and sequestration of the high-silica rhyolitic batches that are assembled upward without the requirement of large batholith underneath. Such reworking leads to significant vertical mass redistribution in the continental crust, which may be relevant to the origin of the continental crust itself. Furthermore, the outlined process of rapid remelting provides a key to understanding the energy-efficient process of generation and eruption of large-volume (“supervolcanic”) quantities of rhyolites in the shallow crust without significant heat loss.

## Acknowledgments

We thank Grants NSF EAR\_CAREER\_0844772, Russian Foundation for Basic Research Grant #07-05-00629. We thank two anonymous reviewers and Mark T Harrison for their insightful comments, and Kathryn Watts and Dana Drew for editing and helpful suggestions that significantly improve the manuscript.

## Appendix A. Supporting information

Supplementary data associated with this article can be found in the online version at <http://dx.doi.org/10.1016/j.epsl.2012.04.011>.

## References

- Anderson, A.T., Davis, A.M., Lu, F., 2000. Evolution of the Bishop Tuff rhyolitic magma based on melt and magnetite inclusions and zoned phenocrysts. *J. Petrol.* 41, 449–473.
- Annen, C., Sparks, R.S.J., 2002. Effects of repetitive emplacement of basaltic intrusions on thermal evolution and melt generation in the crust. *Earth Planet. Sci. Lett.* 203, 937–955.
- Annen, C., Blundy, J.D., Sparks, R.S.J., 2006. The genesis of intermediate and silicic magmas in deep crustal hot zones. *J. Petrol.* 47, 505–539.

- Bachmann, O., Bergantz, G.W., 2004. On the origin of crystal-poor rhyolites: extracted from batholithic crystal mushes. *J. Petrol.* 45, 1565–1582.
- Bacon, C.R., Lowenstern, J.B., 2005. Late Pleistocene granodiorite source for recycled zircon and phenocrysts in rhyodacite lava at Crater Lake, Oregon. *Earth Planet. Sci. Lett.* 233, 277–293.
- Beard, J.S., Ragland, P.C., Crawford, M.L., 2005. Reactive bulk assimilation: a model for crust–mantle mixing in silicic magmas. *Geology* 33, 681–684.
- Bindeman, I.N., Valley, J.W., Wooden, J.L., Persing, H.M., 2001. Post-caldera volcanism: in situ measurement of U–Pb age and oxygen isotope ratio in Pleistocene zircons from Yellowstone caldera. *Earth Planet. Sci. Lett.* 189, 197–206.
- Bindeman, I.N., Fu, B., Kita, N.T., Valley, J.W., 2008. Origin and evolution of Yellowstone silicic magmatism based on ion microprobe analysis of isotopically-zoned zircons. *J. Petrol.* 49, 163–193.
- Bindeman, I.N., Schmitt, A.K., Valley, J.W., 2006. U–Pb zircon geochronology of silicic tuffs from Timber Mt Caldera complex, Nevada: rapid generation of large volume magmas by shallow-level remelting. *Contrib. Mineral. Petrol.* 152, 649–665.
- Bindeman, I.N., Gurenko, A., Carley, T., Miller, C., Martin, E., Sigmarsson, O., 2012. Silicic magma petrogenesis in Iceland by remelting of hydrothermally-altered crust based on oxygen isotope diversity and disequilibria between zircon and magma with implications for MORB. *Terra Nova*, 24, 227–232. <http://dx.doi.org/10.1111/j.1365-3121.2012.01058>.
- Boroughs, S.B., Wolff, J., Bonnicksen, B., Godchaux, M., Larson, P., 2005. Large volume, low- $\delta^{18}\text{O}$  rhyolites of the central Snake River Plain, Idaho, USA. *Geology* 33, 821–824.
- Bowen, N.L., 1928. *The Evolution of Igneous Rocks*. Princeton University Press, Princeton.
- Brandeis, G., Marsh, B.D., 1990. Transient magmatic convection prolonged by solidification. *Geophys. Res. Lett.* 17, 1125–1128.
- Brugger, C.R., Johnston, A.D., Cashman, K.V., 2003. Phase relations in silicic systems at one-atmosphere pressure. *Contrib. Mineral. Petrol.* 146, 356–369.
- Carley, T.L., Miller, C.F., Wooden, J.L., Bindeman, I.N., Barth, A.P., 2011. Zircon from historic eruptions in Iceland: reconstructing storage and evolution of silicic magmas. *Mineral. Petrol.* 102, 135–161.
- Carrigan, C.R., 1988. Biot number and thermos bottle effect: implication for magma chamber convection. *Geology* 16, 771–774.
- Christiansen, E.H., McCurry, M., 2008. Contrasting origins of Cenozoic silicic volcanic rocks from the western Cordillera of the United States. *Bull. Volcanol.* 70, 251–267.
- Coleman, D.S., Gray, W., Glazner, A.F., 2004. Rethinking the emplacement and evolution of zoned plutons: geochronologic evidence for incremental assembly of the Tuolumne Intrusive Suite, California. *Geology* 32, 433–436.
- Davaille, A., Jaupart, C., 1993. Transient high-Rayleigh-number thermal convection with large viscosity variations. *J. Fluid Mech.* 253, 141–166.
- Dufek, J., Bergantz, G.W., 2005. Lower crustal magma genesis and preservation: a stochastic framework for the evaluation of basalt–crust interaction. *J. Petrol.* 46, 2167–2195.
- Dungan, M.A., Davidson, J.P., 2004. Partial assimilative recycling of the mafic plutonic roots of arc volcanoes: an example from the Chilean Andes. *Geology* 32, 773–776.
- Ellis, B.S., Barry, T., Branney, M.J., Wolff, J.A., Bindeman, I., Wilson, R., Bonnicksen, B., 2010. Petrologic constraints on the development of a large-volume, high temperature, silicic magma system. The Twin Falls eruptive centre, central Snake River Plain. *Lithos* 120, 475–489, [10.1016/j.lithos.2010.09.008](http://dx.doi.org/10.1016/j.lithos.2010.09.008).
- Frederick, A., Ochs, F.A., Rebecca, A.Lange, 1997. The partial molar volume, thermal expansivity, and compressibility of  $\text{H}_2\text{O}$  in  $\text{NaAlSi}_3\text{O}_8$  liquid: new measurements and an internally consistent model. *Contrib. Mineral. Petrol.* 129, 155–165.
- Gerya, T., 2009. *Introduction to Numerical Geodynamic Modelling*. Cambridge University Press 358 pp.
- Girard, G., Stix, J., 2010. Rapid extraction of discrete magma batches from a large differentiating magma chamber: the Central Plateau Member rhyolites, Yellowstone Caldera, Wyoming. *Contrib. Mineral. Petrol.* 160, 441–465.
- Glazner, A.F., Bartley, J.M., Coleman, D.S., Gray, W., Taylor, R.Z., 2004. Are plutons assembled over millions of years by amalgamation from small magma chambers? *GSA Today* 14, 4–11.
- Hildreth, W., Wilson, C.J.N., 2007. Compositional zoning of the Bishop Tuff. *J. Petrol.* 48, 951–999.
- Holtz, F., Roux, J., Ohlhorst, S., Behrens, H., Schulze, F., 1999. The effects of silica and water on the viscosity of hydrous quartzofeldspatic melts. *Am. Mineral.* 84, 27–36.
- Huber, C., Bachmann, O., Dufek, J., 2010. The limitations of melting on the reactivation of silicic mushes. *J. Volcanol. Geotherm. Res.* 195, 97–105.
- Huppert, H.E., Sparks, R.S.J., 1988. The generation of granitic magmas by intrusion of basalt into continental crust. *J. Petrol.* 29, 599–624.
- Jaupart, C., Brandeis, G., 1986. The stagnant bottom layer of convecting magma chambers. *Earth Planet. Sci. Lett.* 80, 183–199.
- Leeman, W.P., Oldow, J.J., Hart, W.K., 1992. Lithospheric-scale thrusting in the western U.S. Cordillera as constrained by Sr and Nd isotopic transitions in Neogene volcanic rocks. *Geology* 20, 63–66.
- Lenardic, A., Moresi, L., 2003. Thermal convection below a conducting lid of variable extent: heat flow scalings and two-dimensional, infinite Prandtl number numerical simulations. *Phys. Fluids* 15, 455–466.
- Lipman, P.W., 1984. The roots of ash-flow calderas in western North America: windows into the tops of granitic batholiths. *J. Geophys. Res.* 89 (B10), 8801–8841.
- McCurry, M., Hayden, K.P., Morse, L.H., Mertzman, S., 2008. Genesis of post-hotspot, A-type rhyolite of the E Snake River Plain volcanic field by extreme fractional crystallization of olivine tholeiite. *Bull. Volcanol.* 70, 361–383.
- McCurry, M., Rogers, D.W., 2009. Mass-transfer along the Yellowstone hotspot track I: petrologic constraints on volume of mantle-derived magma. *J. Volcanol. Geotherm. Res.* 118, 86–98.
- Miller, J.S., Wooden, J.L., 2004. Residence, resorption and recycling of zircons in Devils Kitchen Rhyolite, Coso Volcanic Field, California. *J. Petrol.* 45, 2155–2170.
- Nash, B.P., Perkins, M.E., Christensen, J.N., Lee, D.C., Halliday, A.N., 2006. The Yellowstone hotspot in space and time: Nd and Hf isotopes in silicic magmas. *Earth Planet. Sci. Lett.* 247, 143–156.
- Newman, A.V., Dixon, T.H., Gourmelen, N., 2006. A four-dimensional viscoelastic deformation model for Long Valley Caldera, California, between 1995 and 2000. *J. Volcanol. Geotherm. Res.* 150, 244–269.
- Peng, X., Humphreys, E.D., 1998. Crustal velocity structure across the eastern Snake River Plain and the Yellowstone swell. *J. Geophys. Res.* 103, 7171–7186.
- Petford, N., Gallagher, K., 2001. Partial melting of mafic (amphibolitic) lower crust by periodic influx of basaltic magma. *Earth Planet. Sci. Lett.* 193, 483–499.
- Reid, M.R., 2003. Timescales of magma transfer and storage in the crust. In: Rudnick, R.L. (Ed.), *The Crust, Treatise on Geochemistry*, vol. 3. Elsevier, Oxford, UK, pp. 167–193.
- Simakin, A.G., Bindeman, I.N., 2008. Evolution of crystal sizes in the series of dissolution and precipitation events in open magma systems. *J. Volcanol. Geotherm. Res.* 177, 997–1010.
- Streck, M.J., Grunder, A.L., 2008. Phenocryst-poor rhyolites of bimodal, tholeiitic provinces: the Rattlesnake Tuff and implications for mush extraction model. *Bull. Volcanol.* 70, 385–401.
- Snyder, D., 2000. Thermal effects of the intrusion of basaltic magma into a more silicic magma chamber and implications for eruption. *Earth Planet. Sci. Lett.* 175, 257–273.
- Turcotte, D.L., Schubert, G., 2002. *Geodynamics*, second ed. Cambridge University Press, 447 pp.
- Tuttle, O.F., Bowen, N.L., 1958. Origin of granite in the light of experimental studies in the system  $\text{NaAlSi}_3\text{O}_8\text{--KAlSi}_3\text{O}_8\text{--SiO}_2\text{--H}_2\text{O}$ . *Geol. Soc. Am. Memoir*, 74.
- Vazquez, J.A., Reid, M.R., 2002. Time scales of magma storage and differentiation of voluminous high-silica rhyolites at Yellowstone caldera, Wyoming. *Contrib. Mineral. Petrol.* 144, 274–285.
- Vazquez, J.A., Kyriazis, S.F., Reid, M.R., Sehler, R.C., Ramos, F.C., 2009. Thermochemical evolution of young rhyolites at Yellowstone: evidence for a cooling but periodically replenished postcaldera magma reservoir. *J. Volcanol. Geotherm. Res.* 188, 186–196.
- Wallace, P.J., Anderson, A.T., Davis, A.M., 1999. Gradients in  $\text{H}_2\text{O}$ ,  $\text{CO}_2$ , and exsolved gas in a large-volume silicic magma system: interpreting the record preserved in melt inclusions from the Bishop Tuff. *J. Geophys. Res.-Solid Earth* 104, 20097–20122.
- Wark, D.A., Hildreth, W., Spear, F.S., Cherniak, D.J., Watson, E.B., 2007. Pre-eruption recharge of the Bishop magma system. *Geology* 35, 235–238.
- Watts, K., Bindeman, I.N., Shmitt, A.K., 2011. Large-volume rhyolite genesis in caldera complexes of the Snake River Plain: insights from the Kilgore Tuff of the Heise volcanic field, Idaho, with comparison to Yellowstone and Bruneau-Jarbridge rhyolites. *J. Petrol.* 52, 857–890.
- Watts, K.E., Leeman, W.P., Bindeman, I.N., Larson, P.B., 2010. Supereruptions of the Snake River Plain: two-stage derivation of low- $\delta^{18}\text{O}$  rhyolites from normal- $\delta^{18}\text{O}$  crust as constrained by Archean xenoliths. *Geology* 38, 503–506.
- Whitaker, M.L., Nekvasil, H., Lindsley, D.H., McCurry, M., 2008. Can crystallization of olivine tholeiite give rise to potassic rhyolites? an experimental investigation. *Bull. Volcanol.* 70, 417–434.
- Whittington, A.G., Bouhifd, M.A., Richet, P., 2009. The viscosity of hydrous  $\text{NaAlSi}_3\text{O}_8$  and granitic melts: configurational entropy models. *Am. Mineral.* 94, 1–16.
- Zellmer, G.F., Annen, C., Charlier, B.L.A., George, R.M.M., Turner, S.P., Hawkesworth, C.J., 2005. Magma evolution and ascent at volcanic arcs: constraining petrogenetic processes through rates and chronologies. *J. Volcanol. Geotherm. Res.* 140, 171–191.
- Zhang, Y., Walker, D., Leshner, C.E., 1989. Diffusive crystal dissolution. *Contrib. Mineral. Petrol.* 102, 492–513.